# Twist-angle dependent dehybridization of momentum-indirect excitons in $MoSe_2/MoS_2$ heterostructures

2D Materials

PAPER

# Twist-angle dependent dehybridization of momentum-indirect excitons in $MoSe_2/MoS_2$ heterostructures

Nikodem Sokolowski[1], Swaroop Palai[1], Mateusz Dyksik[2], Katarzyna Posmyk[1,2], Michał Baranowski[2], Alessandro Surrente[2], Duncan Maude[1], Felix Carrascoso[3], Onur Cakiroglu[3], Estrella Sanchez[3], Alina Schubert[3], Carmen Munuera[3], Takashi Taniguchi[4], Kenji Watanabe[5], Joakim Hagel[6], Samuel Brem[7], Andres Castellanos-Gomez[3], Ermin Malic[6,7] and Paulina Plochocka[1,2,*]

[1] Laboratoire National des Champs Magnétiques Intenses, UPR 3228, CNRS-UGA-UPS-INSA, Grenoble and Toulouse, France
[2] Department of Experimental Physics, Faculty of Fundamental Problems of Technology, Wroclaw University of Science and Technology, Wroclaw, Poland
[3] Materials Science Factory, Instituto de Ciencia de Materiales de Madrid (ICMM-CSIC), Madrid E-28049, Spain
[4] International Center for Materials Nanoarchitectonics, National Institute for Materials Science, Tsukuba, Ibaraki 305-004, Japan
[5] Research Center for Functional Materials, National Institute for Materials Science, Tsukuba, Ibaraki 305-004, Japan
[6] Department of Physics, Chalmers University of Technology, 412 96 Gothenburg, Sweden
[7] Department of Physics, Philipps University of Marburg, 35037 Marburg, Germany
* Author to whom any correspondence should be addressed.

**E-mail:** paulina.plochocka@lncmi.cnrs.fr

**Keywords:** moiré, interlayer exciton, heterostructure, transition metal dichalcogenide, photoluminescence, twist angle, $MoSe_2/MoS_2$

Supplementary material for this article is available online

OPEN ACCESS

RECEIVED
30 March 2023

REVISED
15 May 2023

ACCEPTED FOR PUBLICATION
6 June 2023

PUBLISHED
16 June 2023



## Abstract

The moiré superlattice has emerged as a powerful way to tune excitonic properties in two-dimensional van der Waals structures. However, the current understanding of the influence of the twist angle for interlayer excitons (IXs) in heterostructures is mainly limited to momentum-direct $K$–$K$ transitions. In this work, we use a judicious combination of spectroscopy and many-particle theory to investigate the influence of the twist angle on momentum-indirect IXs of a $MoSe_2/MoS_2$ heterostructure. Here, the energetically lowest state is a dark and strongly hybridized ΓK exciton. We show that increasing the twist angle from an aligned structure (0° or 60°) gives rise to a large blue shift of the IX, which is a manifestation of the strong dehybridization of this state. Moreover, for small twist angle heterostructures, our photoluminescence measurements reveal contributions from two IX states, which our modelling attributes to transitions from different moiré minibands. Our finding contributes to a better fundamental understanding of the influence of the moiré pattern on the hybridization of momentum-dark IX states, which may be important for applications in moiré-tronics including novel quantum technologies.

## 1. Introduction

Two-dimensional (2D) van der Waals crystals, with their inherent weak interlayer bonding, have enabled a new paradigm of heterostructure engineering [1, 2]. For 2D materials, lattice-matching constraints are no longer obstacles (in contrast to the case of epitaxial heterostructures), while the twist angle between the layers provides a convenient handle to tune their electronic properties, facilitating access to exotic physics phenomena [3–13]. A prominent example is provided by the transition metal dichalcogenides (TMDs) homo- and heterostructures. These represent a unique system in which spin, valley, excitonic, and many-body physics are heavily intertwined and investigated [3, 9–21]. Initially, these heterostructures were described as simple type II quantum wells with electrons and holes located in the adjacent TMD layers. This band alignment leads to the formation of the interlayer exciton (IX) [14,19, 22–26]. However, more detailed investigations of this excitonic complex have quickly shown that the simple type II quantum well picture is not sufficient to capture all of the intriguing physics of TMD heterostructures.

Currently, it is generally accepted that the opto-electronic properties of TMD stacks are determined by the interplay of two effects: (*i*) the formation of a moiré pattern [7, 8, 16–18, 20, 27–30], and

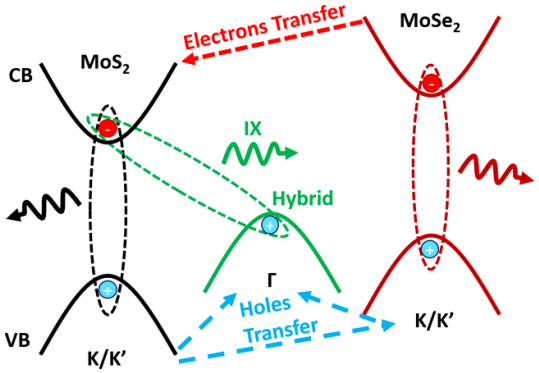


**Figure 1.** Schematic picture of electron and holes transfer between different valleys in a $MoSe_2/MoS_2$ heterostructure. The two intralayer excitons and the hybridized interlayer exciton are indicated by red/black and green ovals, respectively.

(*ii*) the interlayer hybridization of the states [31–36]. A moiré pattern is created due to the mismatch of the TMD lattice constants and/or to the twist between two adjacent layers. It results in a slowly varying periodic potential, which can be treated as an in-plane superlattice of quantum dots [16, 20, 28], which affects locally the optical selection rules [17, 18, 37]. On the other hand, the hybridization arises from the overlap of the atomic wave functions of the two adjacent layers. Therefore, it mostly affects states derived from the chalcogen atomic orbitals, such as the states around the Γ point in the Brillouin zone. This interlayer coupling is well recognized for the TMD homobilayers (and thicker forms) as it is responsible for their indirect band gap character [38–40]. Band structure modelling shows that a similar situation occurs in $MoSe_2/MoS_2$ [41] and $MoS_2/WS_2$ [34] heterostructures, where the hybridization locates the valence band maximum at the Γ point, while the minimum of the conduction band remains at the *K* point (spatially, electrons are located in $MoS_2$), as schematically shown in figure 1. Therefore, the lowest energy excited state is a hybrid exciton, indirect both in real and *k*-space [34]. This feature distinguishes these heterostructures from the most often investigated $MoSe_2/WSe_2$ heterostructures, which are well described as type II quantum wells, with the valence and conduction bands extrema located in adjacent layers but still at the same *K* points of the Brillouin zone [34, 42]. Thus, in terms of the band structure, we can expect that $MoSe_2/MoS_2$ and $MoS_2/WS_2$ heterostructures should be more related to TMD homobilayers [33, 43–46], rather than to the direct bandgap $MoSe_2/WSe_2$ stack, which leads to very different optical properties.

As the twist between the layers modifies their spatial separation [47], it is natural to expect that the energy of the hybridized states strongly depends on the twist angle. Simultaneously, states close to *K* points should be only weakly affected by interlayer hopping (coupling), since the corresponding orbital functions are mostly localized on the transition metal atoms situated in the central layer of the chalcogenide-metal-chalcogenide sandwich. These expectations are supported by band structure calculations [33, 34] and corroborated by experimental studies of homobilayers and $MoSe_2/WSe_2$ heterostructure [28, 42–46]. The characteristic feature for the hybridized states (*K*–Γ or *K*–Λ) is a strong blue shift of the IX energy with increasing twist angle (when moving away from high symmetry alignment – 0° or 60°) [43–46], which is absent (very weak) for direct *K*–*K* transitions [28, 42]. While so far the effect of hybridization has been investigated mainly in homobilayers [33, 43–46, 48], here we report on the distinct fingerprint of the hybridized nature of the ground excitonic transition in $MoSe_2/MoS_2$ heterostructures, which distinguishes it from the much more intensively investigated $MoSe_2/WSe_2$ stack. We show that the photoluminescence (PL) spectrum of the $MoSe_2/MoS_2$ heterostructure reveals a strong blue shift of the ground excitonic transition, with increasing twist angle. This can be understood as a process of layer decoupling and dehybridization of the bands, which is fully confirmed by our theoretical modelling. We conclude that the band structure and optical spectrum of the investigated stacks resemble those observed for twisted homobilayers. Finally, we demonstrate that the optical spectrum of the hybridized exciton is affected by the moiré pattern. For highly aligned samples, we observe a double peak structure of the hybridized IX. Our measured excitation power and temperature dependence, together with band structure calculations, suggests that the double peak originates from the state filling of the moiré bands.

## 2. Results and discussion

Atomically thin flakes were obtained by mechanical exfoliation and stacked using a deterministic transfer method [49]. We fabricated six $MoS_2/MoSe_2$ heterostructures with different interlayer twist angle, encapsulated with hexagonal boron nitride (hBN) on a $SiO_2$ substrate (for fabrication details see section 4.1). Figure 2(a) shows an optical microscope image of one of the heterostructures (Sample A, characterized by a twist angle of 57.2°. Details of Samples B–F are in SI. 1–3). The contour of the $MoSe_2$ and $MoS_2$ monolayers are indicated by black and red curves, and the overlap region of the TMD layers is indicated by a green dashed line with chequered pattern. We determine the interlayer twist angle between monolayers by comparing the second harmonic generation (SHG) intensity as well as polarization-resolved SHG of the monolayers and the heterostructure, which are presented in figure S1 [27, 50].

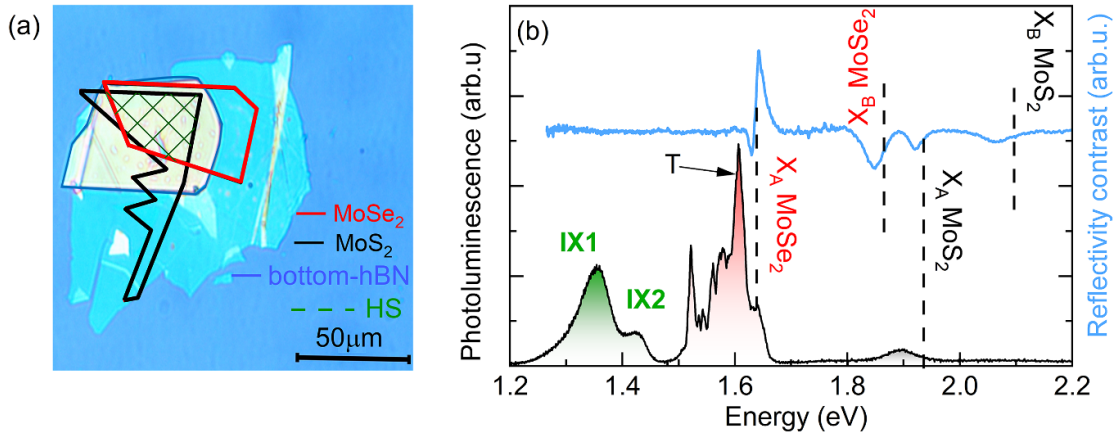


**Figure 2.** (a) Microscope image of the $MoS_2/MoSe_2$ heterostructure encapsulated in hBN. (b) Photoluminescence and reflectivity contrast spectra. The relevant intralayer and interlayer exciton resonances are indicated.

Figure 2(b) shows representative optical spectra from the heterostructure area of sample A. In the reflectivity contrast spectrum (RC), both A and B excitons of $MoS_2$ and $MoSe_2$ are visible. Similarly, in the PL spectrum, we observe emission related to both monolayers. The peak at $\sim 1.9$ eV corresponds to $MoS_2$ and probably stems from a mixture of trion and shallow defect-induced state emission as it is red-shifted by $\sim 35$ meV from the A exciton resonance that is visible in the RC spectra [38, 51, 52]. In the PL spectrum of $MoSe_2$ located between 1.5 and 1.66 eV, we observe a peak corresponding to the free $X_A$ exciton at 1.64 eV and a dominating trion peak $\sim$30 meV below [51, 53], followed probably by some defect state emission.

At lower energies, we observe a pronounced peak at around 1.3–1.4 eV, which is only visible in the heterostructure region. We attribute this emission to the hybridized IX [25, 34, 41], with the electron located at the $K$ point of the $MoS_2$ layer, and the hole located at the hybridized valence band at the $\Gamma$ point of the Brillouin zone [41], as schematically depicted in figure 1. The indirect character of the IX transition, together with the spatial separation of electrons and holes, makes the oscillator strength of the IX transition too weak to be observed in the RC spectra. However, this momentum-dark state can be observed in the PL spectrum due to its high occupation as the energetically lowest state. Its emission is indirect and is driven by phonons, resulting in phonon sidebands [34]. Intriguingly, the IX PL spectrum exhibit a double-peak structure, which is further discussed below. First, we discuss the hybridized nature of the IX exciton in the investigated heterostructure focusing on the dominant low-energy IX PL peak.

Figure 3(a) illustrates the evolution of the PL spectrum for different twist angles. The energy of the PL maximum blue shifts when the twist angle deviates from the 0° or 60° stacking, which corresponds to R-type and H-type stacking, respectively. Fitting the PL peaks with a double Gaussian (dashed lines), we can extract the energy of the ground (dominating) IX1 transition as a function of the twist angle. The shift of the IX1 transition is summarized as open circles in figure 3(b). The blue shift can be as high as 100 meV moving from $\sim$0° to $6-7°$. This strong dependence of the IX emission energy on the twist angle is in stark contrast with the behavior observed in $MoSe_2/WSe_2$ heterostructures [28, 42, 47], where the IX recombination stems from a momentum direct $K$–$K$ transition. This can be explained by the different character of the IX in the $MoSe_2/MoS_2$ heterostructure. The strong blue shift of the IX transition in the $MoSe_2/MoS_2$ heterostructure resembles closely the behavior of IX excitons in twisted homobilayers [33, 43–46], which points to its hybridized nature related to the states close to the $\Gamma$ point.

To obtain a deeper insight into the mechanism driving the evolution of the IX states with the twist angle, we employ the exciton density-matrix formalism, using input fromdensity functional theory (DFT) calculations [8, 33, 34] (see also SI. 6). The Hamiltonian operator of excitons in twisted rigid lattices consists of three different contributions,

$$H \propto E + V(\Theta, r) + T(\Theta, r). \quad (1)$$

Here, $E$ is the exciton dispersion for the decoupled monolayers, $V(\Theta, r)$ is the spatially periodic electrostatic potential and $T(\Theta, r)$ is the hybridization Hamiltonian taking into account the overlapping electronic wave functions giving rise to hybrid exciton states [34]. Similarly to $V(\Theta, r)$, $T(\Theta, r)$ is also spatially periodic as the interlayer distance varies within the moiré supercell. Therefore, both components

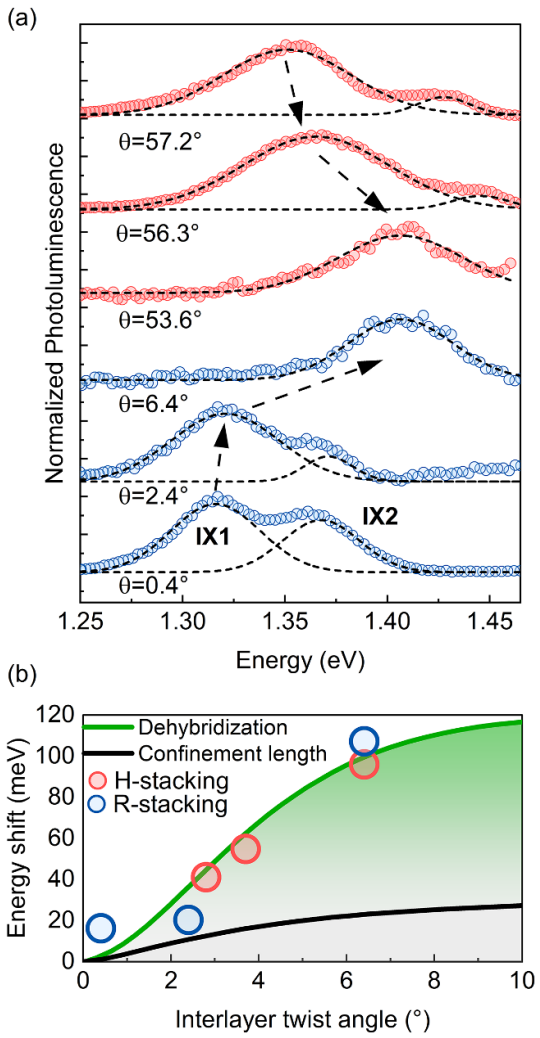


**Figure 3.** (a) Photoluminescence spectra of samples with different twist angles. (b) Calculated energy shift of moiré excitons in R-type stacking taking into account only confinement length (black) and total blue shift including the dehybridization effect (green), which agrees with the shift of the dominating IX1 transition (open circles).

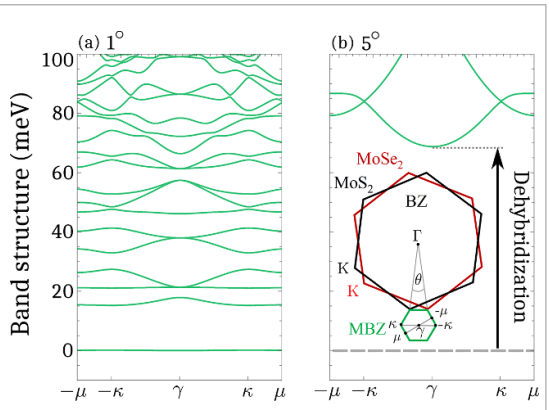


**Figure 4.** Calculated exciton band structure for the $K-\Gamma$ exciton at (a) 1° and (b) 5° twist angle obtained by solving the eigenvalue problem of equation (4). For the lowest twist angle (1°), we observe multiple minibands with the flat lowest-lying band indicating at least one trapped state. With increasing twist angle (5°), the exciton blue shifts, and the multiple band structure vanishes. In addition, the ground state is no longer trapped and exhibits a nearly parabolic dispersion. The inset presents the scheme of the Brillouin zone (BZ) of isolated monolayers and the moiré Brillouin zone (MBZ). The Γ points are chosen to coincide..

determine the twist-angle dependent moiré potential. With the increasing twist angle, the period of the moiré superlattice decreases, which induces delocalization of the IX over many moiré supercells. This results in a spectral blue shift of the exciton transitions [8, 33] (see also figure 4). However, the confinement length increase (the wave function delocalization) gives rise to only a moderate blue shift of the IX transition, as shown by the black curve in figure 3(b). The most significant contribution to the blue shift arises from the increase of the average interlayer distance throughout the supercell when increasing the twist angle. This consequently leads to a significant dehybridization of the moiré excitons and a major blue shift (see also SI. 6). The sum of both, moiré period and dehybridization contributions in R-type stacking, is represented by the green line in figure 3(b), which nicely reproduces the observed blue shift. This result strongly supports the hybrid nature of the IX transition in the $MoSe_2/MoS_2$ heterostructure.

Our model also allows us to explain the double-peak structure of the PL spectrum for small twist angles. The exciton band structure calculations presented in figure 4 show a change in the band dispersion and in the number of bands with the twist angle. For small twist angles (1°), our calculations predict multiple exciton bands separated by several to tens meV. Flat bands indicate that the exciton is spatially localized within the moiré trapping potential [8], while dispersive bands correspond to the spatially delocalized IX. We attribute the double peak structure of IX PL spectrum observed for small twist angles heterostructure to the recombination of excitons related to the different bands. For larger twist angles, the IX exciton band blue shifts and the multiband structure vanishes. This yields a single parabolic delocalized band, which results in a single PL peak.

To support our finding, we have performed measurements as a function of the excitation power. Figure 5(a) shows the normalized PL spectra (from sample B with a 0.4°) for different excitation powers. For the lowest excitation powers, the PL is composed of only one peak. With increasing power, an additional peak on the high energy side emerges. The intensity increases with excitation power for both peaks, as demonstrated in figure 5(b). To quantify this effect, we fit the power dependence of IX1 and IX2 with a power law. The lower energy peak exhibits a sublinear power dependence with an exponent $\alpha_{IX1} = 0.71$, characteristic of a trapping potential (with a low density of states), which experiences a gradual saturation (state filling) with increasing excitation power [14, 37, 54, 55]. The increase of the

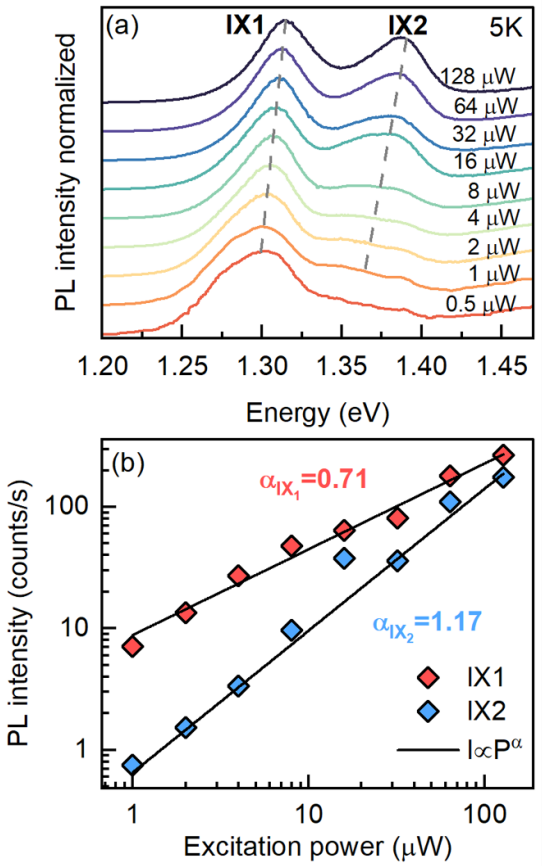


**Figure 5.** (a) Photoluminescence spectra and (b) IX1 and IX2 integrated intensities as a function of the excitation power. The lines are fitted using a power function where $\alpha$ is the exponent.

high energy peak (IX2) with the excitation power is slightly superlinear ($\alpha_{IX2} = 1.17$), which may point to the delocalized exciton character of this transition or to a much higher density of states. Therefore, the power-dependent measurements corroborate the assignment of the double-peak structure to a moiré induced multiband structure of the IX exciton for heterostructures with a small twist angle. In addition, both IX transitions exhibit a blue shift with increasing excitation power (figure S3), which can be attributed to the repulsive dipolar interactions between IXs caused by their permanent out-of-plane dipole moments [56, 57]. To further support our claim, in figure S4 we present the temperature-dependent PL measurements performed on the same sample. With increasing temperature we observe that the IX2-related emission quenches faster as compared to IX1. This observation is consistent with the power-dependent measurements and support the stronger localization of the IX1 transition as compared with IX2.

## 3. Conclusion

Combining experiment and theory, we have shown that the ground exciton state in the $MoSe_2/MoS_2$ heterostructure is a momentum dark and strongly hybridized interlayer ΓK exciton state. Its properties are determined by the combined effect of the moiré potential and the hybridization of $MoS_2$ and $MoSe_2$ valence bands around the Γ point. We observe a strong blue shift of the $K$–Γ transition with increasing twist angle. This can be explained by the dehybridization of the exciton when the twist angle moves away from 0° or 60°. This behavior resembles twisted homobilayers and distinguishes $MoSe_2/MoS_2$ from the most intensively investigated $MoSe_2/WSe_2$ heterostructure. We also show that the multiple peaks we observe in the PL spectrum of $MoSe_2/MoS_2$ heterostructures with a small twist results from the moiré pattern-driven exciton miniband formation.

## 4. Methods

### 4.1. Samples fabrications

TMD monolayers and hBN flakes were obtained by the mechanical exfoliation technique. The TMDs and part of hBN used in the fabrication are commercially available. Synthetic $MoSe_2$ grown by chemical vapor transport has been purchased from HQ graphene. Natural $MoS_2$ from Molly Hill mine, Québec, Canada, hBN for samples E and F is provided from Japan. For the remaining samples, hBN was purchased from HQ Graphene. For all the exfoliations, we used Nitto tape (Nitto Denko corp. SPV 224). Monolayer thickness of $MoS_2$ and $MoSe_2$ was confirmed by transmittance and reflection measurements before their transfer [58]. The heterostructures were stacked by dry pick-up method [49, 59, 60] and deposited on $SiO_2$ substrates.

### 4.2. Spectroscopy measurements

To perform spectroscopy measurements, the samples were mounted on the cold finger of a helium flow cryostat. All of the measurements were performed at a temperature of $T = 5$ K unless otherwise specified. The excitation laser was focused and the PL was collected by a 50 × microscope objective (Mitutoyo Inc.) having a numerical aperture of 0.55. The resulting spot size had a diameter of approximately $\simeq 1\mu$m. For PL measurements, the excitation was provided by a continuous-wave frequency-doubled solid-state laser emitting at 532 nm. A fs-pulsed Ti:Sapphire laser with an average power of 15 mW was used for SHG measurements. Additionally, for polarization resolved SHG, was polarized by means of a Glan–Thompson polarizer and an achromatic half-wave plate. The polarization state of the second harmonic signal was controlled by making use of the same half-wave plate and was analyzed by a linear polarizer. The reflectance, PL and SHG signals were spectrally resolved by a 30 cm long monochromator equipped with a 150 grooves $mm^{-1}$ grating and detected by a liquid nitrogen cooled CCD camera.

### 4.3. Theory

In order to obtain access to the moiré exciton energy landscape we consider a Hamiltonian formulated in second quantization. For this purpose, we start in a decoupled monolayer basis and take into account the moiré potential as periodic modifications to the decoupled exciton energies [8, 33, 61]. Importantly, in the rigid lattice case we have two components of the moiré potential [48, 61]: the electrostatic alignment shift [8] and interlayer hybridization [33, 34, 61]. The decoupled exciton energies are obtained by solving the Wannier equation [22], which gives us the binding energies for the intra/IX states. This allows us to write the Hamiltonian in exciton basis as [8, 30, 33, 34, 61]

$$H_0 = \sum_{LQ\boldsymbol{\xi}} E^{\boldsymbol{\xi}}_{LQ} X^{\boldsymbol{\xi}\dagger}_{L,Q} X^{\boldsymbol{\xi}}_{L,Q} + \sum_{LQ\boldsymbol{\xi},\boldsymbol{g}} V^{\boldsymbol{\xi}}_{L}(\boldsymbol{g}) X^{\boldsymbol{\xi}\dagger}_{L,Q+\boldsymbol{g}} X^{\boldsymbol{\xi}}_{L,Q} + \sum_{LL',\boldsymbol{Q}\boldsymbol{\xi}\boldsymbol{g}} T^{\boldsymbol{\xi}}_{LL'}(\boldsymbol{g}) X^{\boldsymbol{\xi}\dagger}_{L,Q+\boldsymbol{g}} X^{\boldsymbol{\xi}}_{L',Q} + h.c \tag{2}$$

with $L = (l_e, l_h)$ as a compound layer index, $\boldsymbol{Q}$ as the center-of-mass momentum, $\boldsymbol{\xi} = (\xi_e, \xi_h)$ as the exciton valley index and $\boldsymbol{g} = \boldsymbol{G}_2 - \boldsymbol{G}_1$ as the reciprocal lattice vectors of the rigid superlattice (given by the difference of the reciprocal lattice vectors of the two different layers). Additionally, $X^{(\dagger)}$ are annihilation (creation) operators for the non-hybrid excitons. Here, $E^{\boldsymbol{\xi}}_{LQ}$ is the non-hybridized exciton dispersion that is calculated from the Wannier equation [22]. Furthermore, $V^{\boldsymbol{\xi}}_{L}(\boldsymbol{g})$ is the periodic electrostatic shift of the moiré excitons, determined by the local atomic alignment [8]. In this work, the predominant component of the moiré potential stems from the exciton hybridization that is described by the tunneling term in the Hamiltonian reading [33, 34]

$$T^{\boldsymbol{\xi}}_{LL'}(\boldsymbol{g}) = \Big[\delta_{l_h,l'_h}(1-\delta_{l_e,l'_e}) t^{c\boldsymbol{\xi}_e}_{l_e l'_e}(\boldsymbol{g}) \mathcal{F}^{\boldsymbol{\xi}}_{LL'}(\beta_{LL'}\boldsymbol{g}) - \delta_{l_e,l'_e}(1-\delta_{l_h,l'_h}) t^{v\boldsymbol{\xi}_h}_{l_h l'_h}(\boldsymbol{g}) \mathcal{F}^{*\boldsymbol{\xi}}_{LL'}(-\alpha_{LL'}\boldsymbol{g})\Big]. \tag{3}$$

Here, $\mathcal{F}^{\boldsymbol{\xi}}_{LL'}(\boldsymbol{q}) = \sum_{\boldsymbol{k}} \Psi^{\boldsymbol{\xi}*}_{L}(\boldsymbol{k}) \Psi^{\boldsymbol{\xi}}_{L'}(\boldsymbol{k}+\boldsymbol{q})$ are the exciton form factors. Furthermore, we have introduced $\alpha_{ij}(\beta_{ij}) = m^{c(v)}_{i(j)}/(m^c_i + m^v_j)$ with the masses extracted from [62]. The Kronecka deltas ensure single carrier tunneling processes. Furthermore, $t^{\lambda\xi_\lambda}_{l_\lambda l'_\lambda}(\boldsymbol{g})$ are the Fourier coefficients of the real-space tunneling potential, where $\lambda = (c, v)$ is the band index. The Fourier coefficients take into account the twist-angle dependence of the tunneling strength (cf. figure S5).

We transform equation (2) to a zone-folded hybrid moiré exciton basis [8, 33, 61], $Y^{\dagger}_{\boldsymbol{\xi}\eta\boldsymbol{Q}} = \sum_{\boldsymbol{g}L} \mathcal{C}^{\boldsymbol{\xi}\eta*}_{L\boldsymbol{g}}(\boldsymbol{Q}) X^{\boldsymbol{\xi}\dagger}_{L,\boldsymbol{Q}+\boldsymbol{g}}$, where $\boldsymbol{Q}$ is now restricted to the first mini-Brillouin zone. Here, $\eta$ is the new exciton band index, $\mathcal{C}^{\boldsymbol{\xi}\eta*}_{L\boldsymbol{g}}(\boldsymbol{Q})$ are the mixing coefficients determining the relative mixing between sub-bands and intra/IXs. Moreover, $Y^{\dagger}_{\boldsymbol{\xi}\eta\boldsymbol{Q}}$ is the zone-folded moiré exciton creation operator. Consequently, we obtain the following eigenvalue problem

$$E^{\boldsymbol{\xi}}_{LQ}(\boldsymbol{g}) \mathcal{C}^{\boldsymbol{\xi}\eta}_{L\boldsymbol{g}}(\boldsymbol{Q}) + \sum_{\boldsymbol{g}'} V^{\boldsymbol{\xi}}_{L}(\boldsymbol{g}'-\boldsymbol{g}) \mathcal{C}^{\boldsymbol{\xi}\eta}_{L\boldsymbol{g}'}(\boldsymbol{Q}) + \sum_{L'\boldsymbol{g}'} T^{\boldsymbol{\xi}}_{LL'}(\boldsymbol{g}'-\boldsymbol{g}) \mathcal{C}^{\boldsymbol{\xi}\eta}_{L'\boldsymbol{g}'}(\boldsymbol{Q}) = \mathcal{E}^{\boldsymbol{\xi}}_{\eta\boldsymbol{Q}} \mathcal{C}^{\boldsymbol{\xi}\eta}_{L\boldsymbol{g}}(\boldsymbol{Q}). \tag{4}$$

Solving equation (4) numerically gives a microscopic access to the final hybrid moiré exciton energies $\mathcal{E}^{\boldsymbol{\xi}}_{\eta\boldsymbol{Q}}$.

## Data availability statement

All data that support the findings of this study are included within the article (and any supplementary files).

## Acknowledgments

This work received funding from the European Union's Horizon 2020 research and innovation program under Grant Agreements 956813 (2Exciting) and 755655 (ERC-St G 2017 project 2D-TOPSENSE). M B acknowledges National Science Centre Poland within the SONATA BIS program (Grant No. 2020/38/E/ST3/00194) and OPUS LAP (2021/43/I/ST3/01357). Funding was also received from the Ministry of Science and Innovation (Spain) through the Project PID2020-115566RB-I00 and the EU FLAG-ERA project 'To2Dox' under the program PCI2019-111893-2. This study has been partially supported through the EUR Grant NanoX no ANR-17-EURE-0009 in the framework of the 'Programme des Investissements d'Avenir'. M D acknowledges the support from the Polish National Agency for Academic Exchange (Grant No. BPN/BKK/2021/1/00002/U/00001). E M acknowledges support from the European Unions Horizon 2020 research and innovation programme under Grant Agreement No. 881603 (Graphene Flagship) as well as Deutsche Forschungsgemeinschaft (DFG, German Research Foundation) via SFB 1083 (Project B9) and DFG Project 504846924. K W and T T acknowledge support from JSPS KAKENH I (Grant Nos. 19H05790, 20H00354 and 21H05233).

## ORCID iDs

Mateusz Dyksik https://orcid.org/0000-0003-4945-8795
Michał Baranowski https://orcid.org/0000-0002-5974-0850
Alessandro Surrente https://orcid.org/0000-0003-4078-4965

Estrella Sanchez https://orcid.org/0000-0003-0202-4340
Kenji Watanabe https://orcid.org/0000-0003-3701-8119
Joakim Hagel https://orcid.org/0000-0002-3858-4174
Andres Castellanos-Gomez https://orcid.org/0000-0002-3384-3405
Paulina Plochocka https://orcid.org/0000-0002-4019-6138

## References

[1] Geim A K and Grigorieva I V 2013 Van der Waals heterostructures *Nature* **499** 419–25
[2] Novoselov K, Mishchenko A, Carvalho A and Castro Neto A 2016 2D materials and Van der Waals heterostructures *Science* **353** aac9439
[3] Mueller T and Malic E 2018 Exciton physics and device application of two-dimensional transition metal dichalcogenide semiconductors *npj 2D Mater. Appl.* **2** 29
[4] Jorio A 2022 Twistronics and the small-angle magic *Nat. Mater.* **21** 844–5
[5] Dean C R *et al* 2013 Hofstadter's butterfly and the fractal quantum hall effect in moiré superlattices *Nature* **497** 598–602
[6] Cao Y, Fatemi V, Fang S, Watanabe K, Taniguchi T, Kaxiras E and Jarillo-Herrero P 2018 Unconventional superconductivity in magic-angle graphene superlattices *Nature* **556** 43–50
[7] Alexeev E M *et al* 2019 Resonantly hybridized excitons in moiré superlattices in Van der Waals heterostructures *Nature* **567** 81–86
[8] Brem S, Linderälv C, Erhart P and Malic E 2020 Tunable phases of moiré excitons in Van der Waals heterostructures *Nano Lett.* **20** 8534–40
[9] Tang Y *et al* 2020 Simulation of Hubbard model physics in $WSe_2/WS_2$ moiré superlattices *Nature* **579** 353–8
[10] Regan E C *et al* 2020 Mott and generalized Wigner crystal states in $WSe_2/WSe_2$ moiré superlattices *Nature* **579** 359–63
[11] Xu Y, Liu S, Rhodes D A, Watanabe K, Taniguchi T, Hone J, Elser V, Mak K F and Shan J 2020 Correlated insulating states at fractional fillings of moiré superlattices *Nature* **587** 214–8
[12] Huang X *et al* 2021 Correlated insulating states at fractional fillings of the $WSe_2/WSe_2$ moiré lattice *Nat. Phys.* **17** 715–9
[13] Perea-Causin R, Erkensten D, Fitzgerald J M, Thompson J J, Rosati R, Brem S and Malic E 2022 Exciton optics, dynamics and transport in atomically thin semiconductors *APL Mater.* **10** 100701
[14] Rivera P *et al* 2015 Observation of long-lived interlayer excitons in monolayer $MoSe_2$–$WSe_2$ heterostructures *Nat. Commun.* **6** 6242
[15] Rivera P, Yu H, Seyler K L, Wilson N P, Yao W and Xu X 2018 Interlayer valley excitons in heterobilayers of transition metal dichalcogenides *Nat. Nanotechnol.* **13** 1004–15
[16] Yu H, Liu G-B, Tang J, Xu X and Yao W 2017 Moiré excitons: from programmable quantum emitter arrays to spin-orbit–coupled artificial lattices *Sci. Adv.* **3** e1701696
[17] Wu F, Lovorn T and MacDonald A 2018 Theory of optical absorption by interlayer excitons in transition metal dichalcogenide heterobilayers *Phys. Rev.* B **97** 035306
[18] Wu F, Lovorn T and MacDonald A H 2017 Topological exciton bands in moiré heterojunctions *Phys. Rev. Lett.* **118** 147401
[19] Rivera P, Seyler K L, Yu H, Schaibley J R, Yan J, Mandrus D G, Yao W and Xu X 2016 Valley-polarized exciton dynamics in a 2D semiconductor heterostructure *Science* **351** 688–91
[20] Seyler K L, Rivera P, Yu H, Wilson N P, Ray E L, Mandrus D G, Yan J, Yao W and Xu X 2019 Signatures of moiré-trapped valley excitons in $MoSe_2/WSe_2$ heterobilayers *Nature* **567** 66–70
[21] Smoleński T *et al* 2021 Signatures of Wigner crystal of electrons in a monolayer semiconductor *Nature* **595** 53–57
[22] Ovesen S, Brem S, Linderälv C, Kuisma M, Korn T, Erhart P, Selig M and Malic E 2019 Interlayer exciton dynamics in Van der Waals heterostructures *Commun. Phys.* **2** 23
[23] Kang J, Tongay S, Zhou J, Li J and Wu J 2013 Band offsets and heterostructures of two-dimensional semiconductors *Appl. Phys. Lett.* **102** 012111
[24] Miller B, Steinhoff A, Pano B, Klein J, Jahnke F, Holleitner A and Wurstbauer U 2017 Long-lived direct and indirect interlayer excitons in Van der Waals heterostructures *Nano Lett.* **17** 5229–37
[25] Baranowski M *et al* 2017 Probing the interlayer exciton physics in a $MoS_2/MoSe_2/MoS_2$ Van der Waals heterostructure *Nano Lett.* **17** 6360–5
[26] Merkl P *et al* 2019 Ultrafast transition between exciton phases in Van der Waals heterostructures *Nat. Mater.* **18** 691–6
[27] Zhang N, Surrente A, Baranowski M, Maude D K, Gant P, Castellanos-Gomez A and Plochocka P 2018 Moiré intralayer excitons in a $MoSe_2/MoS_2$ heterostructure *Nano Lett.* **18** 7651–7
[28] Tran K *et al* 2019 Evidence for moiré excitons in Van der Waals heterostructures *Nature* **567** 71–75
[29] Jin C *et al* 2019 Observation of moiré excitons in $WSe_2/WSe_2$ heterostructure superlattices *Nature* **567** 76–80
[30] Schmitt D *et al* 2022 Formation of moiré interlayer excitons in space and time *Nature* **608** 499–503
[31] Wilson N R *et al* 2017 Determination of band offsets, hybridization and exciton binding in 2D semiconductor heterostructures *Sci. Adv.* **3** e1601832
[32] Fang H *et al* 2014 Strong interlayer coupling in Van der Waals heterostructures built from single-layer chalcogenides *Proc. Natl Acad. Sci.* **111** 6198–202
[33] Brem S, Lin K-Q, Gillen R, Bauer J M, Maultzsch J, Lupton J M and Malic E 2020 Hybridized intervalley moiré excitons and flat bands in twisted $WSe_2$ bilayers *Nanoscale* **12** 11088–94
[34] Hagel J, Brem S, Linderälv C, Erhart P and Malic E 2021 Exciton landscape in Van der Waals heterostructures *Phys. Rev. Res.* **3** 043217
[35] Merkl P *et al* 2020 Twist-tailoring coulomb correlations in Van der Waals homobilayers *Nat. Commun.* **11** 2167
[36] Tagarelli F *et al* 2023 Electrical control of hybrid exciton transport in a Van der Waals heterostructure *Nat. Photon.* 1–7
[37] Tan Q, Rasmita A, Zhang Z, Novoselov K and Gao W-B 2022 Signature of cascade transitions between interlayer excitons in a moiré superlattice *Phys. Rev. Lett.* **129** 247401
[38] Splendiani A, Sun L, Zhang Y, Li T, Kim J, Chim C-Y, Galli G and Wang F 2010 Emerging photoluminescence in monolayer $MoS_2$ *Nano Lett.* **10** 1271–5
[39] Kuc A, Zibouche N and Heine T 2011 Influence of quantum confinement on the electronic structure of the transition metal sulfide $TS_2$ *Phys. Rev.* B **83** 245213
[40] Raja A *et al* 2018 Enhancement of exciton–phonon scattering from monolayer to bilayer $WSe_2$ *Nano Lett.* **18** 6135–43
[41] Su X, Ju W, Zhang R, Guo C, Zheng J, Yong Y and Li X 2016 Bandgap engineering of $MoS_2/MX_2$ ($MX_2 = WS_2$, $MoSe_2$ and $WSe_2$) heterobilayers subjected to biaxial strain and normal compressive strain *RSC Adv.* **6** 18319–25
[42] Choi J *et al* 2021 Twist angle-dependent interlayer exciton lifetimes in Van der Waals heterostructures *Phys. Rev. Lett.* **126** 047401
[43] Villafañe V, Kremser M, Hübner R, Petrić M M, Wilson N P, Stier A V, Müller K, Florian M, Steinhoff A and Finley J J 2023 Twist-dependent intra-and interlayer excitons in moiré $MoSe_2$ homobilayers *Phys. Rev. Lett.* **130** 026901

[44] Yan W, Meng L, Meng Z, Weng Y, Kang L and Li X-A 2019 Probing angle-dependent interlayer coupling in twisted bilayer $WS_2$ *J. Phys. Chem.* C **123** 30684–8
[45] Van Der Zande A M *et al* 2014 Tailoring the electronic structure in bilayer molybdenum disulfide via interlayer twist *Nano Lett.* **14** 3869–75
[46] Liu K, Zhang L, Cao T, Jin C, Qiu D, Zhou Q, Zettl A, Yang P, Louie S G and Wang F 2014 Evolution of interlayer coupling in twisted molybdenum disulfide bilayers *Nat. Commun.* **5** 4966
[47] Nayak P K *et al* 2017 Probing evolution of twist-angle-dependent interlayer excitons in $MoSe_2$/$WSe_2$ Van der Waals heterostructures *ACS Nano* **11** 4041–50
[48] Linderälv C, Hagel J, Brem S, Malic E and Erhart P 2022 The moiré potential in twisted transition metal dichalcogenide bilayers (arXiv:2205.15616)
[49] Castellanos-Gomez A, Buscema M, Molenaar R, Singh V, Janssen L, Van Der Zant H S and Steele G A 2014 Deterministic transfer of two-dimensional materials by all-dry viscoelastic stamping *2D Mater.* **1** 011002
[50] Hsu W-T, Zhao Z-A, Li L-J, Chen C-H, Chiu M-H, Chang P-S, Chou Y-C and Chang W-H 2014 Second harmonic generation from artificially stacked transition metal dichalcogenide twisted bilayers *ACS Nano* **8** 2951–8
[51] Cadiz F *et al* 2017 Excitonic linewidth approaching the homogeneous limit in $MoS_2$-based Van der Waals heterostructures *Phys. Rev.* X **7** 021026
[52] Mak K F, He K, Shan J and Heinz T F 2012 Control of valley polarization in monolayer $MoS_2$ by optical helicity *Nat. Nanotechnol.* **7** 494–8
[53] Ross J S *et al* 2013 Electrical control of neutral and charged excitons in a monolayer semiconductor *Nat. Commun.* **4** 1474
[54] Kremser M, Brotons-Gisbert M, Knörzer J, Gückelhorn J, Meyer M, Barbone M, Stier A V, Gerardot B D, Müller K and Finley J J 2020 Discrete interactions between a few interlayer excitons trapped at a $MoSe_2$–$WSe_2$ heterointerface *npj 2D Mater. Appl.* **4** 8
[55] Li W, Lu X, Wu J and Srivastava A 2021 Optical control of the valley Zeeman effect through many-exciton interactions *Nat. Nanotechnol.* **16** 148–52
[56] Nagler P *et al* 2017 Interlayer exciton dynamics in a dichalcogenide monolayer heterostructure *2D Mater.* **4** 025112
[57] Brotons-Gisbert M, Baek H, Campbell A, Watanabe K, Taniguchi T and Gerardot B D 2021 Moiré-trapped interlayer trions in a charge-tunable $WSe_2$/$MoSe_2$ heterobilayer *Phys. Rev.* X **11** 031033
[58] Frisenda R *et al* 2017 Micro-reflectance and transmittance spectroscopy: a versatile and powerful tool to characterize 2D materials *J. Phys. D: Appl. Phys.* **50** 074002
[59] Rebollo I, Rodrigues-Machado F, Wright W, Melin G and Champagne A 2021 Thin-suspended 2D materials: facile, versatile and deterministic transfer assembly *2D Mater.* **8** 035028
[60] Haley K L, Cloninger J A, Cerminara K, Sterbentz R M, Taniguchi T, Watanabe K and Island J O 2021 Heated assembly and transfer of Van der Waals heterostructures with common nail polish *Nanomanufacturing* **1** 49–56
[61] Hagel J, Brem S and Malic E 2022 Electrical tuning of moiré excitons in $MoSe_2$ bilayers *2D Mater.* **10** 014013
[62] Kormányos A, Burkard G, Gmitra M, Fabian J, Zólyomi V, Drummond N D and Fal'ko V 2015 k·p theory for two-dimensional transition metal dichalcogenide semiconductors *2D Mater.* **2** 022001